Phosphorene analogues: Isoelectronic two-dimensional group-IV monochalcogenides with orthorhombic structure

Lídia C. Gomes and A. Carvalho
Centre for Advanced 2D Materials and Graphene Research Centre, National University of Singapore, 6 Science Drive 2, 117546 Singapore

(Received 19 April 2015; revised manuscript received 18 June 2015; published 6 August 2015)

The group-IV monochalcogenides SnS, SnSe, GeS, and GeSe form a family within the wider group of semiconductor "phosphorene analogues." Here, we used first-principles calculations to investigate systematically their structural, electronic, and optical properties, analyzing the changes associated with the reduction of dimensionality, from bulk to monolayer or bilayer form. We show that all those binary phosphorene analogues are semiconducting, with band-gap energies covering part of the infrared and visible range, and in most cases higher than phosphorene. Further, we found that they have multiple valleys in the valence and conduction band, the latter with spin-orbit splitting of the order of 19–86 meV.

DOI: 10.1103/PhysRevB.92.085406 PACS number(s): 73.90.+f

I. INTRODUCTION

Two-dimensional (2D) materials have been extensively studied ever since a monolayer graphene was isolated by mechanical exfoliation [1]. Thereafter, the interest was promptly extended to other 2D materials, such as hexagonal boron nitride (h-BN), layered metal dichalcogenides (LMDCs), and phosphorene, to name a few [2–4]. In special phosphorene, a monolayer of black phosphorus adopts an orthorhombic structure different from graphene and transition-metal dichalcogenides [5,6]. This anisotropic structure is the origin of some of phosphorene's interesting properties, such as superior flexibility under tensile strain [7] and giant thermoelectric coefficient [8].

However, the waved structure of phosphorene is shared by yet another class of 2D materials that has so far eluded attention. In the bulk form, group-IV monochalcogenides GeS, GeSe, SnS, and SnSe all assume structures that can be considered derivatives of the orthorhombic black phosphorus [9], belonging to the space group $Pcmn - D_{2h}^{16}$ (lower than black phosphorus, which has only one element and therefore belongs to $Bmab - D_{2h}^{18}$). This is the α phase of SnS, also known as herzenbergite, a naturally occurring but rare mineral.[1]

Currently the most important prospective application of α-SnS is as an absorber material for film photovoltaic (PV) cells. Although other chalcogenide materials such as CdTe and $CuInGaSe_2$ also show high PV efficiencies [11–13], many factors make their usage difficult such as the high cost and toxicity of Cd [11,14,15]. In contrast, SnS is made of abundant and nontoxic elements, and its optical band gap of $\sim$1.3 eV [11,16] is right in the range of the optimal values for solar cells (1.1 to 1.5 eV). Moreover, according to a recent study, solar conversion efficiencies achieved so far for SnS can be well beyond the potential limit for the material due to the poor choice of band alignment in the devices [17]. In addition, group-IV monochalcogenides may appear to be superior to other 2D semiconductors in properties where anisotropy plays an important role, as demonstrated in the record thermoelectric coefficient recently reported for SnSe ($ZT = 2.6$ at 923 K) [18].

In addition, these binary "phosphorene analogues" are expected to reveal distinct intrinsic properties in monolayer form, as some of the lattice symmetry operations, including inversion, are only present in bulk and in even-numbered layer systems. In this sense, they are different from phosphorene [19], where inversion symmetry prevents spin-orbit (SO) splitting. In contrast, as shown in the present article, group-IV monochalcogenide monolayers show a large intrinsic spin-orbit splitting at valence- and conduction-band valleys. However, even though a few theoretical and experimental works have reported on the electronic and optical properties of monolayer or few-layer SnS [11,20], monolayer properties of this group remain poorly explored.

In this work, we use first-principles calculations to investigate electronic, structural, and optical properties of the four aforementioned group-IV monochalcogenides MX, with $M =$ (Sn, Ge) and $X =$ (S, Se), in the phosphorenelike α phase. We compare the properties of monolayer and bilayer with those of bulk for each of these materials, highlighting the differences in the electronic and optical properties.

II. METHODS

We use first-principles calculations based on density functional theory to obtain the electronic, structural, and optical properties of monochalcogenides. We employ a first-principles approach based on Kohn-Sham density functional theory (KS-DFT) [21], as implemented in the QUANTUM ESPRESSO code [22]. The exchange-correlation energy is described by the generalized gradient approximation (GGA) using the Perdew-Burke-Ernzerhof (PBE) [23] functional. Interactions between valence and core electrons are described by Troullier-Martins pseudopotentials [24]. The Kohn-Sham orbitals were expanded in a plane-wave basis with a cutoff energy of 70 Ry and, for the charge density, a cutoff of 280 Ry was used. The Brillouin zone (BZ) was sampled

[1]Some of these compounds (at least SnS and SnSe) have a more symmetric β phase, with space symmetry $Cmcm - D_{2h}^{17}$, at higher temperature [10]. However, according to our calculations, all four compounds are most stable in the α phase on the monolayer form.

using a Γ-centered 10×10×1 grid following the scheme proposed by Monkhorst-Pack [25]. For the optical properties (dielectric constant and conductivity), a finer 40×40×1 grid was employed. The calculation of the spin-orbit splitting was performed using noncollinear calculations with fully relativistic pseudopotentials.

In addition, a hybrid functional approximation for the exchange-correlation term, Heyd-Scuseria-Ernzerhof (HSE06) [26], was employed in order to give reliable results for the gap energies, which are well known to be underestimated when employing semilocal GGA approximations. For the hybrid functional band structure calculations, we used the Vienna *ab initio* simulation package (VASP) [27,28] with the projector augmented wave potentials [29]. An energy cutoff of 40 Ry was used for the plane-wave basis set and integrations over BZ were performed using samples of 8×8×1 k points for monolayers and bilayers and 8×8×4 k points for bulk structures.

For monolayer and bilayer models, we used periodic boundary conditions along the three dimensions, with vacuum regions of 8 and 9 Å, respectively, between adjacent images in the direction perpendicular to the layers. Convergence tests with greater vacuum spacing guarantee that this size is enough to avoid spurious interaction between neighboring images.

The optical conductivity was calculated directly from the joint density of states, i.e., taking into account only direct excitations. The real part of the dielectric function is then calculated using the Kramers-Kronig relationship.

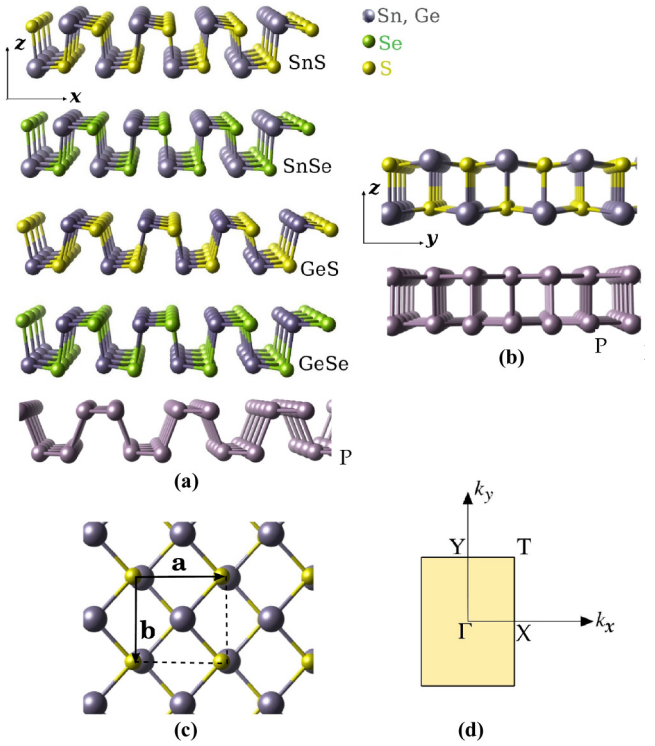

FIG. 1. (Color online) Optimized structures of monolayers of group-IV monochalcogenides with phosphorenelike structure. (a) Side view of the x-z plane for the four compounds and for phosphorene. (b) Side view of the y-z plane of SnS and phosphorene. (c) Top view of the structures, with the lattice vectors **a** and **b** along the x and y directions. (d) The respective BZ and the high-symmetry points Γ, X, T, and Y.

III. RESULTS

A. Crystal structure

The bulk α phase has an orthorhombic structure with eight atoms per primitive unit cell, four of each species. The primitive unit cell contains two puckered layers, stacked on top of each other. The bilayer is obtained by increasing the lattice supercell vector perpendicular to the plane of the layers. The monolayer has four atoms per unit cell, as in Fig. 1(c). Each atomic species is covalently bonded to three neighbors of the other atomic species, forming zigzag rows of alternating elements. Thus, there is in each atom a lone pair pushing its three bonds towards a tetrahedral coordination, just like in black phosphorus, resulting in its characteristic waved structure.

We adopt the axes system used by previous works [15,30,31], where layers are chosen to sit on the x-y plane, i.e., perpendicular to the z direction. This is the same system conventionally used for black phosphorus, which takes the y axis to be parallel to the puckering direction. Each layer has three nontrivial symmetry operations, namely a vertical mirror plane parallel to the x-z plane, a twofold screw rotation along an axis parallel to y, and a glide reflection on a plane parallel to the x-y plane. The atomic positions, in units of the unit cell vectors **a**, **b**, and **c**, are $\pm(x,\frac{1}{4},z;\ \frac{1}{2}+z,\frac{1}{4},\frac{1}{2}-x)$. For bulk SnS, for example, our calculated fractional atomic coordinates are $x(\mathrm{Sn}) = z(\mathrm{Sn}) = 0.12$, $x(\mathrm{S}) = 0.48$, and $z(\mathrm{S}) = 0.85$. The lattice parameters and fractional atomic positions do not deviate much from those in the parent black-phosphorus structure. As can be seen in Fig. 1(a), the most noticeable difference is that the height of the atoms (along z) is no longer constant; rather, cation and anion have slightly different heights alternating along x. The lattice is also more compact along x, but less compact along the y direction, to decrease the repulsion between the atoms of the same type aligned up along the ripples (Table I). Full details of the structure of the other compounds, including the calculated $x(M,X)$ and $z(M,X)$, can be found in the Supplemental Material (SM) [32].

The calculated lattice parameters are in good agreement with experimental data for bulk SnS (**a** = 4.33 Å, **b** = 3.98 Å, and **c** = 11.20 Å) [9,33] and bulk SnSe (**a** = 4.44 Å, **b** = 4.15 Å, and **c** = 11.50 Å) [34]. Our results are also in agreement with previous theoretical studies of SnS [11,14,35].

TABLE I. Optimized lattice vectors in Å for the α phase of SnS, SnSe, GeS, and GeSe along with those of phosphorene (P).

	Monolayer		Bilayer		Bulk		
	a	**b**	**a**	**b**	**a**	**b**	**c**
SnS	4.24	4.07	4.28	4.05	4.35	4.02	11.37
SnSe	4.36	4.30	4.42	4.25	4.47	4.22	11.81
GeS	4.40	3.68	4.42	3.67	4.40	3.68	10.81
GeSe	4.26	3.99	4.31	3.97	4.45	3.91	11.31
P	4.60	3.30	4.57	3.31	4.57	3.51	11.69

TABLE II. Gap energies (E_g) for monolayer, bilayer, and bulk monochalcogenides and phosphorene from GGA and hybrid functional calculations. We compare results from QUANTUM ESPRESSO (QE) and VASP codes for the GGA approach. The star (*) indicates direct band gaps. Experimental values from previous works are also shown. All values are given in eV.

	Monolayer			Bilayer			Bulk			
	GGA QE	GGA VASP	HSE VASP	GGA QE	GGA VASP	HSE VASP	GGA QE	GGA VASP	HSE VASP	Experiment
SnS	1.40	1.38	1.96	1.14	1.12	1.60	0.83	0.82	1.24	1.20–1.37 [15]
SnSe	1.01*	0.96*	1.44*	0.79	0.76	1.20	0.55	0.54	1.00	0.898 [30], 0.95 [36]
GeS	1.69	1.65	2.32	1.55	1.55	2.20	1.24	1.22	1.81	1.70–1.96 [15]
GeSe	1.14*	1.18*	1.54*	1.02*	0.98*	1.45*	0.59	0.57	1.07	1.14 [37]
P	0.90		1.66	0.55		1.30	0.07		0.39	0.33 [38–40]

It is interesting to note that the lattice parameters show little variation among the four compounds, differing less than 7%. This is due to the similar electronegativity of Se and S, and of Ge and Sn, and, consequently, to the similar bond strengths. Thus, the lattice parameter trend is mostly dominated by the ionic radius of the constituents, the most compact structure being that of GeS. The lattice parameters of the sulfides remain nearly unchanged for different number of layers, while those of the selenides show variations of $\sim\pm 2\%$.

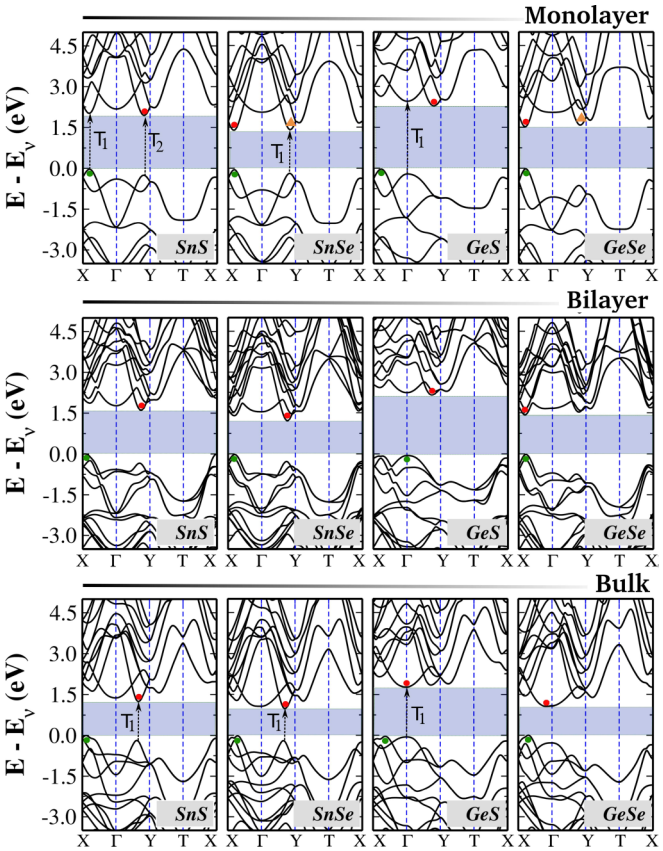

FIG. 2. (Color online) Electronic band structures for monolayer, bilayer, and bulk group-IV monochalcogenides calculated using the HSE hybrid functional. The VBM and CBM are highlighted by full circles. Dashed black arrows indicate possible direct transitions (T_1 and T_2) to points very close in energy to the VBM and CBM. Triangles indicate the position of the CBM when spin-orbit coupling effects are considered.

B. Electronic properties of monolayer, bilayer, and bulk models

A tunable band-gap energy within the visible range is one of the most interesting properties of the group-IV monochalcogenides. The calculated values for the energy gaps (E_g) are summarized in Table II. These were obtained by calculating the band structures using the HSE functional along the high-symmetry paths of the Brillouin zone (BZ) [Fig. 1(d)]. The HSE exchange-correlation functional opens the gap, compared to the PBE band structure, while the band dispersion remains nearly unchanged.

Some aspects of the band structure are common to all systems studied. The dispersion of the bands nearest to the gap is nearly the same along the Γ-X and Γ-Y directions, despite the striking difference between the structure along those two crystallographic directions. This is probably due to the Sn-5s (Ge-4s) character of those bands. Additionally, in most cases, there are multiple valence-band and conduction-band valleys, and most of the compounds have an indirect gap, except for monolayer SnSe, bulk GeS, and monolayer and bilayer GeSe, as shown by our calculated band structures in Fig. 2 and by the positions of the VBM and CMB in the BZ (Table III). This is different from black phosphorus and phosphorene, which have a well-defined direct or nearly direct gap. Finally, as expected, E_g decreases with increasing number of layers.

In the following, we examine in detail the band structure of each one of the compounds. The energy gaps given were obtained with the HSE functional, unless otherwise stated, and without considering spin-orbit coupling. Last, we will consider the spin-orbit splitting.

TABLE III. (Δ_{k_x}; Δ_{k_y}): Positions of the VBM and CBM along the Γ-X and Γ-Y lines in the BZ. The values are given in units of $2\pi/|\mathbf{a}|$ and $2\pi/|\mathbf{b}|$ for $\hat{k}_x$ and $\hat{k}_y$ directions, respectively.

		Monolayer	Bilayer	Bulk
SnS	CBM	(0.00 ; 0.84)	(0.00 ; 0.74)	(0.00 ; 0.70)
	VBM	(0.22 ; 0.00)	(1.00 ; 0.00)	(0.12 ; 0.00)
SnSe	CBM	(0.20 ; 0.00)	(0.00 ; 0.78)	(0.00 ; 0.72)
	VBM	(0.20 ; 0.00)	(0.20 ; 0.00)	(0.30 ; 0.00)
GeS	CBM	(0.00 ; 0.82)	(0.00 ; 0.76)	(0.00 ; 0.00)
	VBM	(0.26 ; 0.00)	(1.00 ; 0.00)	(0.40 ; 0.00)
GeSe	CBM	(0.20 ; 0.00)	(0.20 ; 0.00)	(0.80 ; 0.00)
	VBM	(0.20 ; 0.00)	(0.20 ; 0.00)	(0.30 ; 0.00)

(a) SnS has an indirect gap independently of the number of layers. The indirect band gaps calculated with HSE are $E_g = 1.96$, 1.60, and 1.24 eV for monolayer, bilayer, and bulk SnS, respectively. The results for bulk agree very well with the experimental measured gap energies compiled in Ref. [15], which presents band-gap energies obtained from optical absorption measurements and extrapolated to zero temperature around 1.2–1.3 eV, agreeing very well with our calculated values. Another previous study [41] found a band gap of 1.11 eV for bulk using HSE06, but, different from our study, they used the experimental lattice parameters as input. The excellent agreement between the calculated HSE band gap and the experimental energies is unexpected, since the gap measured in optical experiments differs from the conduction gap by the exciton binding energy, which can be of the order of hundreds of meV in two-dimensional materials [6]. However, previous theoretical studies using the GW method [42,43] obtained $E_g = 2.57$, 1.57, and 1.07–1.26 eV for monolayer, bilayer, and bulk SnS, respectively [11,15]. This variation in the GW gaps may be due to the difficulty in treating the screening in 2D materials [44]. The agreement is very good except for monolayer, and this difference may be due to several factors. One of them is the presence of shallow core d bands in SnS, as discussed in Ref. [17].

We now turn to the details of the band structure. In all cases (monolayer, bilayer, and bulk), the valence-band maxima (VBM) and conduction-band minima (CBM) are located along the Γ-X and Γ-Y lines. In the monolayer, there are other competing local CBM and VBM, very close in energy to the band edges. By considering this, in addition to the indirect band gap observed for the monolayer, two direct gaps higher in energy by 75 meV (represented by transition T_1 in Fig. 2), and 0.22 eV (T_2) are also identified along Γ-X and Γ-Y lines, respectively. For the bulk, we also observe a competing point along the Γ-Y line, defining a direct gap of 1.40 eV. The situation is similar for the other compounds studied (Table IV).

(b) SnSe. For monolayer SnSe, the direct gap of 1.44 eV is calculated along the Γ-X line. A second maxima at 0.16 eV above VBM is obtained in the Γ-Y direction, defining an additional direct transition at 1.60 eV (T_1). The bilayer band structure shows some differences. The CBM is now in the Γ-Y direction and the material is characterized by an indirect gap of 1.20 eV, with the VBM located in the Γ-X direction.

For the bulk model, the CBM is also along the Γ-Y direction, and an indirect gap of 1.00 eV is defined with the VBM in the Γ-X direction. In this case, the second point nearest in energy to the VBM, lower in energy by 0.17 eV, is located along Γ-Y and defines a direct gap of 1.17 eV (T_1 in Fig. 2). Both indirect and direct calculated gaps agree very well with the experimentally estimated values of 0.95 and 1.15 eV from Ref. [36].

TABLE IV. Smallest direct gaps obtained from the HSE calculations. The respective transitions are indicated by black arrows in Fig. 2. The values are given in eV.

	Monolayer		Bulk
	T_1	T_2	T_1
SnS	2.03	2.18	1.40
SnSe	1.60		1.17
GeS	2.62		1.83

(c) GeS. Monolayer GeS has an indirect band gap of 2.32 eV. This is defined by the CMB and VBM along the Γ-Y and the Γ-X lines. The lowest-energy direct transition is at the Γ point (T_1 in Fig. 2). This direct gap is only 0.3 eV higher in energy than the indirect gap. In bilayer GeS, the gap is also indirect and 0.12 eV lower in energy than that of the monolayer. The CBM in this case is still along Γ-Y, but the VBM is at the Γ point. A second VB maximum at the X point is almost degenerate in energy with the VBM at Γ.

Bulk GeS has an indirect gap of 1.81 eV. The direct gap at the Γ point is only 20 meV higher in energy than the indirect one. Our results are in excellent agreement with the bulk GeS gap energies extrapolated to zero temperature given in Ref. [15], which range from 1.70 to 1.96 eV for different experiments.

(d) GeSe. For GeSe monolayer, our calculations produce a direct gap $E_g = 1.54$ eV along the Γ-X line. For the bilayer structure, a direct gap of 1.45 eV is found in the Γ-X direction, near the X point.

Similar to mono- and bilayer GeSe, the electronic structure for the bulk also shows the VBM and CBM in the Γ-X direction. However, the calculated gap of 1.07 eV is indirect in this case, as the CBM is located closer to the Γ point. In this case, our calculations are also in very good agreement with experimental results, where optical measurements have indicated bulk GeSe as an indirect band-gap semiconductor with $E_g = 1.14$ eV [37].

Spin-orbit splitting

In the case of monolayer, the spin-orbit coupling gives rise to a splitting of the bands. This is different from monolayer phosphorene, where the inversion symmetry, together with time-reversal symmetry, require that the bands for the two spins are degenerate. No spin-orbit splitting is expected in bulk and even-numbered layer group-IV monochalcogenides, for the same reason.

In order to quantify the effect of SO coupling, a fully relativistic calculation based on GGA was performed for the monolayer of all compounds. Figure 3 shows the calculated electronic bands for monolayer SnSe with and without spin-orbit coupling. The results for the other materials, given in SM, are very similar. So, for the sake of simplicity, we discuss only the SnSe case.

The spin degeneracy of the bands is lifted in all BZ except along Γ-X, the direction along which the C_2 rotational symmetry and the xz mirror symmetry are preserved. Otherwise, the SO coupling hardly changes the shape of the bands, except for band crossings avoided in the relativistic result. However, the absolute minimum of the conduction band is along Γ-Y for all systems. For SnSe, the conduction band splits by 52 meV near the Y point (at the Γ-Y line). This defines a new CBM, since the other maxima at the Γ-X direction shifts by only 38 meV. The same occurs for GeSe, for which a split of 50 meV for the valley near Y is calculated. The VBM remains along Γ-X in all cases. The calculated spin-orbit splittings are large for the conduction bands of all the phosphorene analogues, with the largest calculated value being for the SnS CBM (86 meV), as

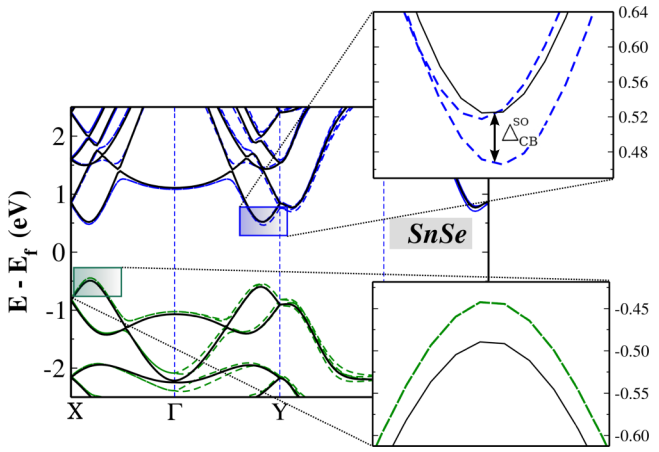

FIG. 3. (Color online) Electronic band structures for SnSe monolayer with (green and blue dashed lines) and without (continuous black lines) spin-orbit coupling effect.

can be seen in the table presented in Fig. 4. This exceeds the spin-orbit splittings for the conduction bands of some of the most used transition-metal dichalcogenides (TMDs), e.g., MoS_2, $MoSe_2$, WS_2, and WSe_2, which have spin-orbit splittings between 3 and 30 meV at the conduction-band valleys [45]. However, the SO split on the valence-band valleys is always smaller than for TMDs, which have splittings of the order of 0.15–0.50 eV [46,47].

C. Optical properties

We now analyze the optical properties of this class of materials, discussing the influence of anisotropy and the consequences of lower dimensionality. The complex dielectric function $\epsilon(\omega)$ of the bulk materials has been measured by electron energy-loss spectroscopy (EELS), optical transmission, and reflectance measurements [48–51]. It can also be obtained from the optical conductivity $\sigma(\omega)$, which is related to ϵ by

$$\epsilon(\omega) = 1 + \frac{i}{\omega\epsilon_0}\sigma(\omega), \quad \sigma(\omega) = -i\omega\epsilon_0[\epsilon(\omega) - 1], \qquad (1)$$

where ω is the frequency of the incoming electromagnetic wave and ϵ_0 is the vacuum permittivity.

	Δ^{SO}_{VB}	Δ^{SO}_{CB}	$\Delta^{SO}_{E_g}$
SnS	8	87	95
SnSe	14	52	85
GeS	1	56	41
GeSe	9	48	48

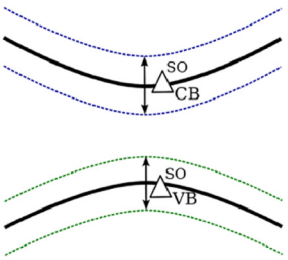

FIG. 4. (Color online) Calculated SO splittings of the CB and VB for the valleys along Γ-Y in meV. The schematic picture shows in continuous black lines the bands without spin-orbit effects, which are taken into account in a fully relativistic calculation. The lifted conduction and valence bands are shown in dashed lines. The lowering in E_g is given by $\Delta^{SO}_{E_g}$.

The imaginary part of the dielectric tensor $\epsilon_i(\omega)_{\alpha,\beta}$ for the bulk system can be obtained from the first-principles band structure using

$$\epsilon_i(\omega)_{\alpha\beta} = \frac{2\pi^2 e^2}{m^2 V}\sum_{i,f}\int \frac{\mathbf{M}_{\alpha\beta}}{[E_f(\mathbf{k}) - E_i(\mathbf{k})]^2} \times \delta[E_f(\mathbf{k}) - E_i(\mathbf{k}) - \hbar\omega]d^3k, \qquad (2)$$

where $E_i(\mathbf{k})$ represents the Kohn-Sham eigenvalues, $\mathbf{M}_{\alpha\beta}$ represents the squared momentum matrix elements, α and β are the crystal directions, and subscripts i and f correspond to initial and final states, respectively. V and m are the cell volume and the electron mass, respectively. Note that this includes only direct transitions.

From Eq. (2), the real part of $\epsilon(\omega)$ can be obtained via the Kramers-Kroning relations:

$$\epsilon_r(\omega)_{\alpha\beta} = 1 + \frac{2}{\pi}\int_0^\infty \frac{\omega'\epsilon_i(\omega')_{\alpha\beta}}{\omega'^2 + \omega^2}d\omega'. \qquad (3)$$

Since the integral over the BZ needs a very large number of points to converge, we use the GGA functional for the calculation of $E_i(\mathbf{k}), E_f(\mathbf{k})$, but subsequently apply a rigid shift to correct the band gap to the value obtained from the HSE calculation.

We start by validating the calculation by comparing $\sigma(\omega)$ obtained for bulk with the respective values extracted from experiment. For all four monochalcogenides, the agreement is excellent, as shown in Fig. 5, which compares the calculated real part of the conductivity $\sigma_(\omega)$ with experimental results from previous works. Both the threshold energy and the bandwidth of the σ_i spectrum, which extends to about 20 eV in all cases, are well reproduced by the calculation. The low-frequency value of the real part, σ_r, is also in reasonable agreement with experiment.

A striking feature is that the dielectric function is nearly isotropic, i.e., the three diagonal components σ_{xx}, σ_{yy}, and σ_{zz} have nearly the same magnitude and spectral dependence. This is a direct consequence of the similar band dispersion along the three respective directions of the BZ, which in turn originates in the structure. As shown in Fig. 1, the *Pcmn* structure can be regarded as a distorted cubic NaCl structure, and the dispersion of the bands near the gap, mostly with s character, is little affected by the symmetry breaking, especially in plane. The nearly isotropic behavior of ϵ is in agreement with previous calculations [49,52], but at variance with experimental data for GeS [48]. This may be due to the difficulty in performing measurements with the electric-field polarization perpendicular to the layers. The nearly isotropic behavior of the optical response is in variance with black phosphorus, which has significantly different absorption thresholds for the two in-plane directions.

Plasmon energies of these materials can also be estimated from the first-principles dielectric function, when $\mathrm{Re}[\epsilon] = 0$. A comparison of the calculated real part of the dielectric function $\epsilon_r(\omega)$ with experimental results from previous works is presented in Fig. 6. The plasmon energies are calculated for the intrinsic (insulating) material, i.e., interband plasmons are considered. The calculated values are in the range 15–20 eV, in excellent agreement with experiment [50], except for the

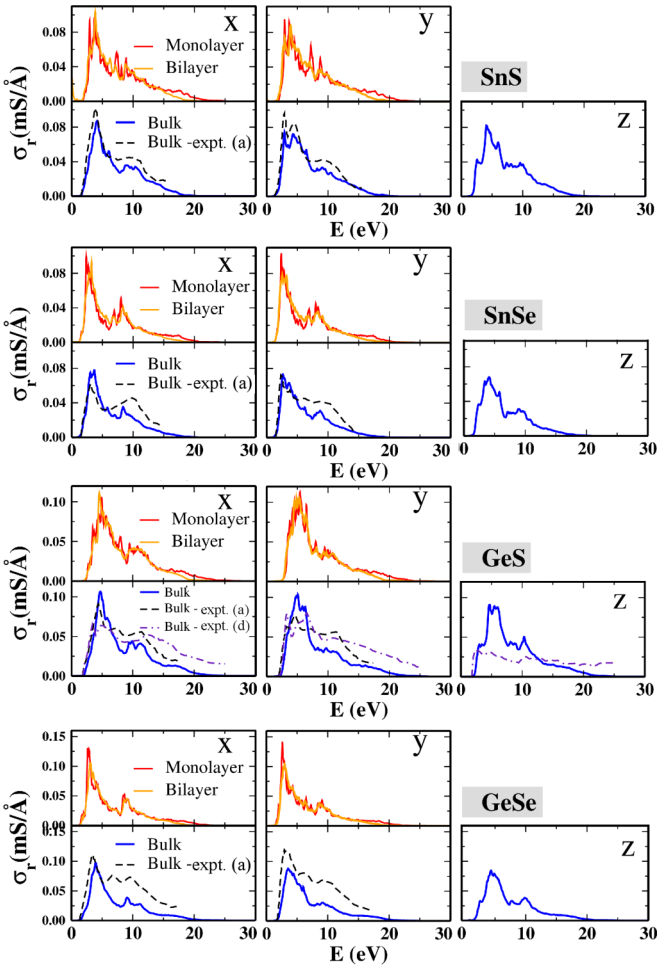

FIG. 5. (Color online) Real part of the optical conductivity $\sigma_r(\omega)$ for monolayer (full red lines), bilayer (full orange lines), and bulk (full blue lines) monochalcogenides. For comparison, experimental results are also included from previous works. As the experimental works report $\epsilon_i(\omega)$, we use relations (1) to obtain $\sigma_r(\omega)$. (a) Ref. [50]; (d) Ref. [48].

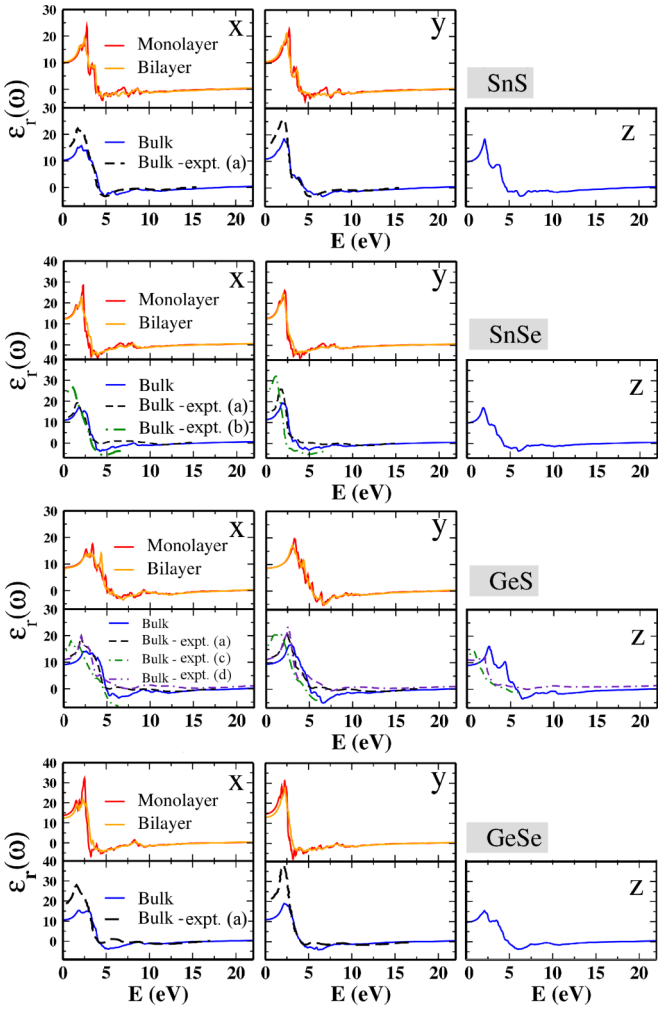

FIG. 6. (Color online) Real part of dielectric constants $\epsilon_r(\omega)$ for monolayer (full red lines), bilayer (full orange lines), and bulk (full blue lines) monochalcogenides. Experimental results from previous works are also included. (a) Ref. [50]; (b) Ref. [51]; (c) Ref. [31]; (d) Ref. [48].

sulfides (Table V) for which the plasmon frequency is slightly overestimated. We also note that although experimentally the plasmon frequency is the same for the three dimensions, there is a slight variation in the theoretical results up to the uncertainty of the calculation. Even so, the experimental results are very well reproduced.

We now compare the optical response of the monolayer and bilayer material with that of the bulk. For two-dimensional materials, the dielectric constant is not well defined, depending

TABLE V. Calculated values of the real part of the dielectric constant at $\omega \to 0$ (ϵ_r^0) and at high-energy limits (ϵ_r^∞). The plasmon frequencies (ω_p) for x and y directions in monolayer and x, y, and z directions in bulk are also presented. For both monolayer and bulk, ϵ_r^∞ assume the same values for all directions, while the static dielectric constant ϵ_r^0 and the plasmon frequency ω_p vary slightly for different directions. Experimental values of ω_p for the bulk of all compounds from Ref. [50] are also included. All values are given in eV.

	Monolayer					Bulk							
	ϵ_r^0		ϵ_r^∞	ω_p		ϵ_r^0			ϵ_r^∞	ω_p			ω_p-Expt.
	x	y	x,y	x	y	x	y	z	x,y,z	x	y	z	x,y,z
SnS	9.9	10.0	0.69	19.3	19.2	10.30	10.94	9.90	0.72	18.1	17.8	18.0	16.22
SnSe	12.5	12.8	0.77	14.8	14.8	10.90	11.50	9.90	0.78	15.7	15.7	15.9	15.44
GeS	8.7	8.6	0.63	20.4	20.4	9.20	9.45	9.10	0.64	20.2	20.1	20.2	18.21
GeSe	13.8	14.7	0.70	17.2	16.5	10.60	10.96	9.80	0.72	17.7	17.2	17.8	17.30

on the interlayer distance L as [39,53,54]

$$\epsilon = 1 + \frac{4\pi\chi_{2D}}{L}. \quad (4)$$

The 2D polarizability χ_{2D} is constant, and can be obtained from the first-principles calculations, where ϵ is calculated from Eq. (2) by integrating over the whole supercell. The interlayer distance L in that case thus corresponds to the supercell length along the direction perpendicular to the layers [6]. Hence, direct comparison between the 2D and 3D systems is not possible unless L is defined. Here, in order to obtain effective monolayer and bilayer dielectric constants comparable with bulk, thus highlighting the differences originating in the band structure and lower dimensionality, we take L to be the bulk interlayer distance $|\mathbf{a}|/2$, thus defining $\epsilon_{\text{eff}} = 1 + (\epsilon - 1)\frac{L}{a/2}$.

Comparing the effective optical conductivity for monolayer, bilayer, and bulk, we notice that the spectral dependence and magnitude are very similar; however, as the number of layers decreases, the peaks get sharper, due to the divergence of the joint density of states for saddle points of $E_f(\mathbf{k}) - E_i(\mathbf{k})$ [55]. The real part of ϵ is also nearly unchanged for effective interlayer spacing equal to that of bulk. More details of the points of interest in the spectra are given in Table V.

IV. CONCLUSIONS

We have performed a systematic study of the electronic and optical properties of the family of phosphorene analogues SnS, SnSe, GeS, and GeSe, and explored the consequences of lower dimensionality and symmetry breaking.

One of the most interesting facets of these materials is that from bulk down to monolayer, they cover a wide range of band-gap energies, from ∼1.0 to 2.3 eV according to hybrid functional calculations. The band gap increases as the number of layers is reduced, thus making it possible to extend the absorption edge up to the green region of the spectrum.

In parallel, this family of materials has the advantage of showing little variation in lattice parameters. This makes alloying a very promising direction for tuning the optical and electronic character of the materials.

Further, the smallest lattice mismatch between SnS and GeSe compounds, for both lattice parameters, can be an indication of these materials as good candidates for the formation of hybrid structures [56]. Phosphorene itself has a small lattice mismatch to some of these materials, with which it can be combined.

Additionally, the inversion symmetry breaking in monolayer allows for spin-orbit splitting of the conduction- and valence-band valleys along the Γ-Y direction. This effect is absent in bulk group-IV monochalcogenides and in phosphorene. The spin-orbit splitting can be as large as 86 meV for the conduction-band minimum of SnS. The large spin-orbit splitting is likely due to the s character of the VBM and CBM.

The properties described here open the possibility of using group-IV monochalcogenides for optoelectronics and spintronics. Few-layer isolation by exfoliation has already been achieved [17,20], and it is just a matter of time until control of the layer number becomes possible.

Finally, this illustrates that phosphorene is the parent structure of a whole class of orthorhombic 2D materials, whose potential is to be revealed once they are isolated in monolayer or few-layer form.

ACKNOWLEDGMENTS

The authors acknowledge Professor Antonio Helio Castro Neto for valuable suggestions. This work was supported by the National Research Foundation-Prime Minister's Office, Republic of Singapore, under its Medium Sized Centre Programme and CRP award "Novel 2D materials with tailored properties: beyond graphene" (Grant No. R-144-000-295-281). The first-principles calculations were carried out on the GRC high-performance computing facilities.

[1] K. S. Novoselov, A. K. Geim, S. V. Morozov, D. Jiang, Y. Zhang, S. V. Dubonos, I. V. Grigorieva, and A. A. Firsov, Science **306**, 666 (2004).
[2] Sheneve Z. Butler *et al.*, ACS Nano **7**, 2898 (2013).
[3] Lifeng Wang, Bin Wu, Jisi Chen, Hongtao Liu, Pingan Hu, and Yunqi Liu, Adv. Mater. **26**, 1559 (2014).
[4] Qing Hua Wang, Kourosh Kalantar-Zadeh, Andras Kis, Michael S. Coleman, and Jonathan N. Strano, Nat. Nanotechnol. **7**, 699 (2012).
[5] Han Liu, Adam T. Neal, Zhen Zhu, Zhe Luo, Xianfan Xu, David Tománek, and Peide D. Ye, ACS Nano **8**, 4033 (2014).
[6] A. S. Rodin, A. Carvalho, and A. H. Castro Neto, Phys. Rev. B **90**, 075429 (2014).
[7] Qun Wei and Xihong Peng, Appl. Phys. Lett. **104**, 251915 (2014).
[8] Ruixiang Fei, Alireza Faghaninia, Ryan Soklaski, Jia-An Yan, Cynthia Lo, and Li Yang, Nano Lett. **14**, 6393 (2014).
[9] H. Wiedemeier and H. G. von Schnering, Z. Kristallogr. **156**, 143 (1981).
[10] A. R. H. F. Ettema, R. A. de Groot, C. Haas, and T. S. Turner, Phys. Rev B **46**, 7363 (1992).
[11] Georgios A. Tritsaris, Brad D. Malone, and Efthimios Kaxiras, J. Appl. Phys. **113**, 233507 (2013).
[12] A. Green, K. Emery, Y. Hishikawa, W. Warta, and E. D. Dunlop, Prog. Photovoltaics **20**, 12 (2012).
[13] Repins, M. A. Contreras, B. Egaas, C. DeHart, J. Scharf, C. L. Perkins, B. To, and R. Noufi, Prog. Photovoltaics **16**, 235 (2008).
[14] Julien Vidal, Stephan Lany, Mayeul d'Avezac, Alex Zunger, Andriy Zakutayev, Jason Francis, and Janet Tate, Appl. Phys. Lett. **100**, 032104 (2012).
[15] Brad D. Malone and Efthimios Kaxiras, Phys. Rev B **87**, 245312 (2013).
[16] K. T. Ramakrishna Reddy, N. Koteswara Reddy, and R. W. Miles, Sol. Energy Mater. Sol. Cells **90**, 3041 (2006).
[17] Lee A. Burton and Aron Waish, Appl. Phys. Lett. **102**, 132111 (2013).
[18] Li-Dong Zhao, Shih-Han Lo, Yongsheng Zhang, Hui Sun, Gangjian Tan, Ctirad Uher, C. Wolverton, Vinayak P. Dravid,

and Mercouri G. Kanatzidis, Nature (London) **508**, 373 (2014).
[19] J. Ribeiro-Soares, R. M. Almeida, L. G. Cançado, M. S. Dresselhaus, and A. Jorio, Phys. Rev. B **91**, 205421 (2015).
[20] Bablu Mukherjee, Yongqing Cai, Hui Ru Tan, Yuan Ping Feng, Eng Soon Tok, and Chorng Haur Sow, ACS Appl. Mater. Interfaces **5**, 9594 (2013).
[21] W. Konh and L. J. Sham, Phys. Rev. **140**, A1133 (1965).
[22] P. Giannozzi *et al.*, J. Phys.: Condens. Matter **21**, 395502 (2009).
[23] J. P. Perdew, K. Burke, and M. Ernzerhof, Phys. Rev. Lett. **77**, 3865 (1996).
[24] N. Troullier and J. L. Martins, Phys. Rev. B **43**, 1993 (1991).
[25] H. J. Monkhorst and J. D. Pack, Phys. Rev. B **13**, 5188 (1976).
[26] J. Heyd, G. E. Scuseria, and M. Ernzerhof, J. Chem. Phys. **124**, 219906 (2006).
[27] G. Kresse and J. Furthmüller, Comput. Mater. Sci. **6**, 15 (1996).
[28] G. Kresse and J. Furthmüller, Phys. Rev. B **54**, 11169 (1996).
[29] P. E. Blochl, Phys. Rev. B **50**, 17953 (1994).
[30] M. Parenteau and C. Carlone, Phys. Rev. B **41**, 5227 (1990).
[31] S. Logothetidis, L. Vinna, and M. Cardona, Phys. Rev. B **31**, 2180 (1985).
[32] See Supplemental Material at http://link.aps.org/supplemental/10.1103/PhysRevB.92.085406 for further information on the calculated bond lenghts and electronic band structures with spin-orbit coupling effects.
[33] L. Ehm, K. Knorr, P. Dera, A. Krimmel, P. Bouvier, and M. Mezouar, J. Phys.: Condens. Matter **16**, 3545 (2004).
[34] I. Lefebvre, M. A. Szymanski, J. Olivier-Fourcade, and J. C. Jumas, Phys. Rev. B **58**, 1896 (1998).
[35] S. Alptekina and M. Durandurdu, Solid State Commun. **150**, 870 (2010).
[36] P. A. Fernandes, M. G. Sousa, P. M. P. Salome, J. P. Leitao, and A. F. da Cunha, Crystengcomm **15**, 10278 (2013).
[37] Dimitri D. Vaughn, Romesh J. Patel, Michael A. Hickner, and Raymond E. Schaak, J. Am. Chem. Soc. **132**, 15170 (2010).
[38] R. Keyes, Phys. Rev. **92**, 580 (1953).
[39] D. J. Warschauer, Appl. Phys. **34**, 1853 (1963).
[40] Y. Akahama, S. Endo, and Narita, J. Phys. Soc. Jpn. **52**, 2148 (1983).
[41] Lee A. Burton, Diego Colombara, Ruben D. Abellon, Ferdinand C. Grozema, Laurence M. Peter, Tom J. Savenije, Gilles Dennler, and Aron Walsh, Chem. Mater. **25**, 4908 (2013).
[42] F. Huser, T. Olsen, and K. S. Thygesen, Phys. Rev. B **87**, 235132 (2013).
[43] L. Hedin, Phys. Rev. **139**, A796 (1965).
[44] Falco Huser, Thomas Olsen, and Kristian S. Thygesen, Phys. Rev. B **88**, 245309 (2013).
[45] K. Kośmider, J. W. González, and J. Fernández-Rossier, Phys. Rev. B **88**, 245436 (2013).
[46] Di Xiao, Gui-Bin Liu, Wanxiang Feng, Xiaodong Xu, and Wang Yao, Phys. Rev. Lett. **108**, 196802 (2012).
[47] Gui-Bin Liu, Wen-Yu Shan, Yugui Yao, Wang Yao, and Di Xiao, Phys. Rev. B **88**, 085433 (2013).
[48] J. D. Wiley, W. J. Buckel, W. Braun, G. W. Fehrenbach, F. J. Himpsel, and E. E. Koch, Phys. Rev. B **14**, 697 (1976).
[49] L. Makinistian and E. A. Albanesi, J. Phys.: Condens. Matter **19**, 186211 (2007).
[50] R. Eymard and A. Otto, Phys. Rev. B **16**, 1616 (1977).
[51] S. Logothetidis and H. M. Polatoglou, Phys. Rev. B **36**, 7491 (1987).
[52] L. Makinistian and E. A. Albanesi, Phys. Rev. B **74**, 045206 (2006).
[53] P. Cudazzo, I. V. Tokatly, and A. Rubio, Phys. Rev. B **84**, 085406 (2011).
[54] T. C. Berkelbach, M. S. Hybertsen, and D. R. Reichman, Phys. Rev. B **88**, 045318 (2013).
[55] A. Carvalho, R. M. Ribeiro, and A. H. Castro Neto, Phys. Rev. B **88**, 115205 (2013).
[56] Jiong Lu, Lídia C. Gomes, Ricardo W. Nunes, A. H. Castro Neto, and Kian Ping Loh, Nano Lett. **14**, 5133 (2014).